

---

## **Chapter 6. Study of the UWB GPR**

---

### **6.1. Introduction**

At the start of the HUDEM project in 1996, there was no UWB GPR system commercially available. Therefore we decided to develop a laboratory version of an impulse UWB GPR to investigate the feasibility of enhancing the depth resolution and classification capability of UWB systems. Further the system would provide us with the necessary UWB data for the evaluation of signal- and image processing algorithms, developed by other researchers in the scope of the HUDEM project. In this chapter we will give a detailed description of the system and its acquisition software, together with a study of the antenna set-up and the range performance of the system, using the time domain model from the previous chapter. Finally some raw data on surrogate mines are shown and preliminary results are drawn.

### **6.2. General description of the system**

The components of the laboratory UWB GPR are mainly off-the-shelf laboratory equipment. Only the antennas are developed in the RMA. A schematic representation of the UWB GPR system is given in Fig. 6-1.

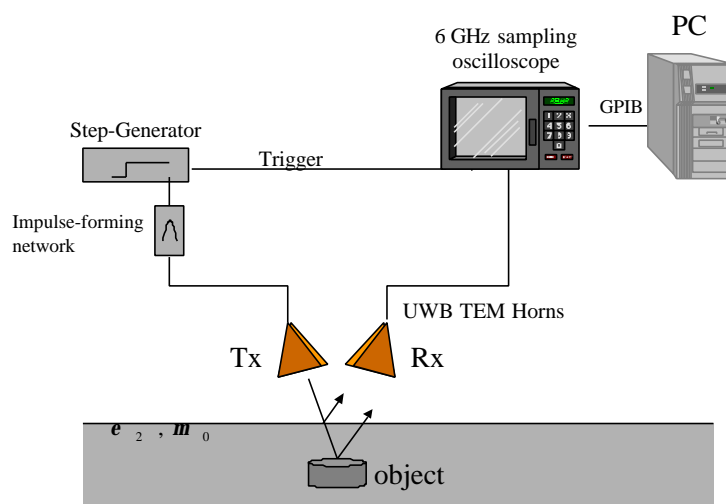


**Fig. 6-1:** Schematic representation of the UWB GPR system

### *Transmitter*

On the transmitting side a Picosecond Pulse Labs step-generator type PSPL 4050B is used, followed by an impulse-forming-network. The PSPL 4050B is a step-generator based on the combination of an avalanche transistor and a Step Recovery Diode (SRD). The avalanche transistor is used as a fast switch, allowing a rapid discharge of the energy stored in a transmission line. The rise time of the generated fast transition is later on enhanced by a SRD. In the PSPL 4050B this SRD is implemented in a box outside the generator as shown in Fig. 6-2.



**Fig. 6-2:** The Picosecond Pulse Labs step-generator, type PSPL 4050B

The pulse repetition frequency (PRF) of the generator can be manually set from 10 Hz to 1 MHz. The delay between the trigger output and the step is adjustable by four switches on the front panel between 0 and 110 ns. The delay uncertainty or jitter of

the generator is inferior to 3 ps [1]. The generated step has an amplitude of 10 V, a very short rise-time and a high waveform purity. The step, recorded by a 20 GHz sampling oscilloscope is shown in Fig. 6-3. The measured rise-time is 60 ps.

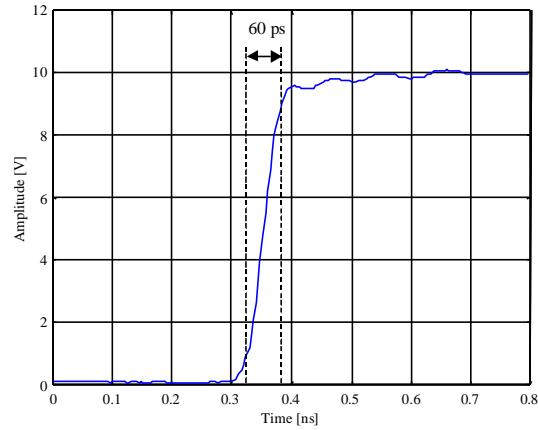


**Fig. 6-3:** Waveform generated by the step-generator PSPL 4050B

The fast transient step is transformed by an impulse-forming-network to a pulse with a maximal amplitude of 2.55 Volts. Experience learned that using a pulse as input signal for the antennas works better than using a step. It limits in time the cross coupling between the antennas. The pulse waveform, measured by a 6 GHz sampling oscilloscope is shown in Fig. 6-4. The Full Width at Half Maximum (FWHM) is 82 ps and the oscillations in the tail of the pulse do not exceed 90 mV or 3.6 % of the full scale.

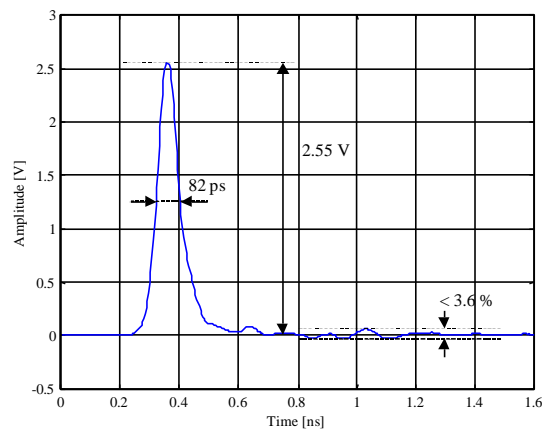


**Fig. 6-4:** Pulse waveform after the impulse-forming-network

### ***Antennas***

The pulse coming from the impulse-forming-network is fed to a pair of two identical TEM horn antennas, with a dielectric filling. A photo of the antennas is shown in Fig. 6-8. The antennas used in the laboratory UWB system are referred to as *Antenna 4* in Chapter 4, Section 4.5. We opted for these antennas because they meet almost all the design goals for the demining application as stated in Chapter 3, Section 3.3. The dimensions of the antennas are small, they are capable of radiating and receiving fast transient pulses without too much ringing and they can be used off-ground. To reduce the ringing in the antennas, a RAM is placed at the outside end of the antenna plates. The normalised IR of the antennas is given in Chapter 4, Fig. 4-10 (d). In the configuration of the UWB GPR, the two antennas are put side by side. More details about the antenna configuration will be given in Section 6.3.

### ***Receiver***

On the receiver side, the 6 GHz sampling oscilloscope TDS820 from Tektronix is used to digitize the backscattered signal. The oscilloscope has only a 14 bit resolution. To increase its dynamic range, the oscilloscope has a possibility of averaging up to 10.000 times. Without averaging, the dynamic range of the oscilloscope would be limited by the 14 bit resolution to 84 dB, while commercial GPR receivers have dynamic ranges of at least 100 dB. A disadvantage of using an oscilloscope is that it has no time-varying gain. As a whole we can say that the oscilloscope is not an ideal receiver for a GPR, but given its bandwidth and its price it was the only realistic solution for the laboratory system. The data coming from the oscilloscope are collected by a computer, using a GPIB bus. The most important technical details of the sampling oscilloscope are resumed in Table 6.1

Name	Description
Number of channels	2
Number of digitising bits	14
Input connector type	SMA
Input impedance	$50 \Omega \pm 1 \Omega$
Sensitivity	2 mV/Div - 200mV/Div
Input range	$\pm 2V$
Random channel noise	$\leq 1.2 \text{ mV RMS}$
Time range	20ps/Div – 2ms/Div
Delayed time base	between 16ns and 20 ms
Delay jitter	$< 9\text{ps}$ for delay of 200 ns
Input bandwidth	6 GHz
Maximum rise time	$57.8 \pm 0.1\text{ps}$ per $^{\circ}\text{C}$
Number of averaging	up to 10.000 times

**Table 6.1:** Technical details of the Tektronix TDS820



**Fig. 6-5:** The Tektronix TDS820 6GHz sampling oscilloscope

### *Total system bandwidth*

To have an idea of the overall bandwidth of the system the two TEM horn antennas are aligned on boresight of each other and the main-beam response is measured. The transmitting antenna is excited with the impulse coming from the impulse-forming-network (see Fig. 6-4). The received signal is recorded by the 6 GHz sampling oscilloscope. Fig. 6-6(a) shows the normalised received voltage as a function of time.

In Fig. 6-6 (b) the power spectrum of this normalised received signal is shown, which gives an idea of the overall bandwidth of the system. The 3 dB frequency band of the whole system (transmitter – antennas - receiver) is from about 1 GHz up to 5 GHz.

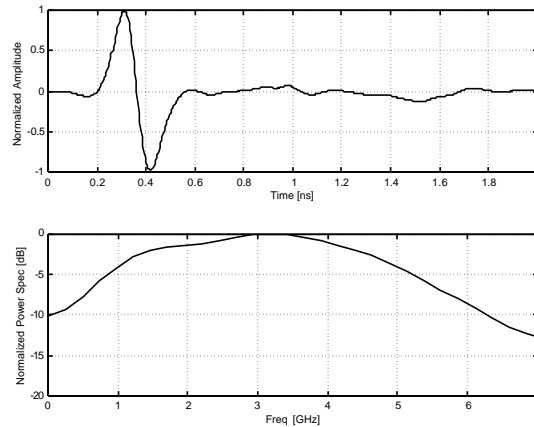


**Fig. 6-6** (a) Normalised amplitude of the main beam response  
(b) Normalised power spectrum of the main beam response

### *XY-scanners*

The antennas of the laboratory UWB GPR can be mounted on two different xy-scanners. In both cases the whole set-up is controlled by a computer, which commands via a serial connection the position of the xy-scanner and meanwhile collects the data (A-scans) from the 6 GHz oscilloscope via a GPIB connection.

The first scanning platform is an indoor xy-table of 2 m by 2.5 m and 2 m high. The xy-table is computer-controlled and has a minimum displacement step of less than 0.1 mm. In the scanning area of the table, two sandboxes are placed, 1.5 m by 1.5 m each and 0.8 m deep. The first one is filled with sand, the second one with loam. The permittivity of both types of soil is fully characterised as a function of frequency and moisture content. The indoor xy-table is represented in Fig. 6-7.



**Fig. 6-7:** Set-up of the UWB GPR system on the indoor xy-table

The second xy-scanner is a small platform, mounted on a robot of the type HUNTER. The robot itself is remote controlled and can be moved in adverse terrain. The scanning area of the platform is 50 cm by 70 cm. The set-up gives the opportunity of doing trials outside. Fig. 6-8 shows a photo of the antennas mounted together with the metal detector on the HUNTER.

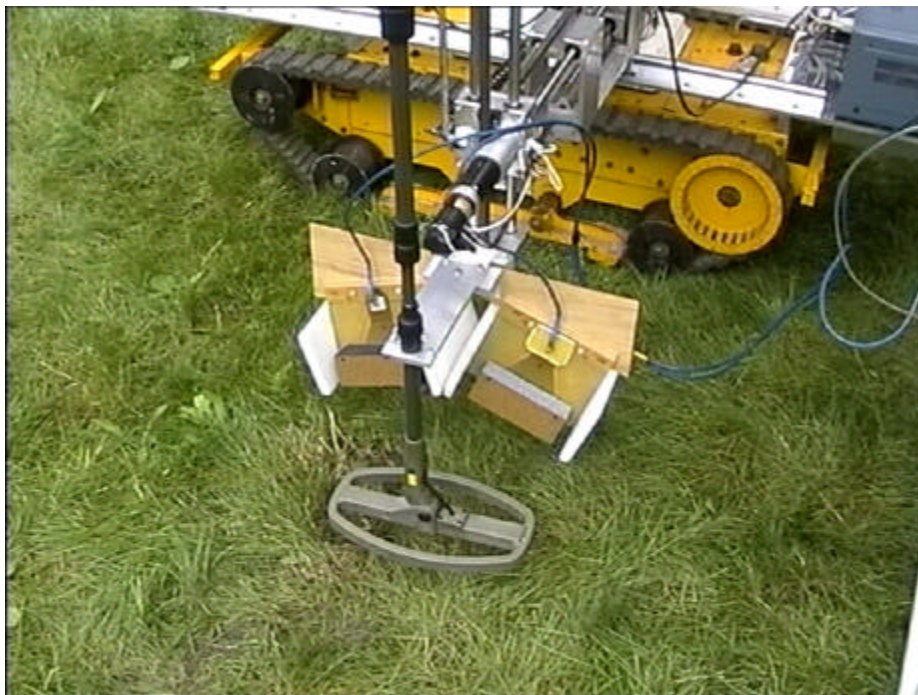


**Fig. 6-8:** Set-up of the UWB GPR system on the HUNTER robot

## 6.3. Study of the antenna configuration

In the design of the laboratory UWB GPR, a study was made to optimise the position and orientation of the Tx and Rx antennas. In commercial GPR systems, the antennas are usually put side by side with their boresight parallel to each other. Putting the antennas side by side seems a logical choice, but whether the parallel boresight is the optimal choice, is not evident. Further, in the demining application we want to use the antennas off ground, so we also have to determine their height.

### 6.3.1. Height above the ground

For the choice of the height of the antennas above the ground, we took into account three factors: the far field of the antenna, the distance from the antennas to the target and the fact that the system will be used in a demining application.

The height of the antennas above the ground is partially dictated by the application. For the demining application the degree of mobility of the antennas must be high. Minefields have often a rough surface and are covered with a lot of vegetation. Therefore we opted to use the antennas not closer than 20 cm to the ground. For the same reason of mobility, the two antennas will be put as close as possible to each other.

A second parameter influencing the choice of the height is the far field of the antennas. In a lot of GPR applications, the antennas are used in the near field. Indeed, to detect an object, the object does not have to be in the far field of the GPR antennas. However, in the time domain model, presented in Chapter 4, we always supposed the objects in the far field of the antennas. If we want to use the time domain model to tune signal processing algorithm, it is better that the antennas operate in the far field. Hence, the knowledge of the far field region becomes important. In Chapter 4, an alternative definition of the far-field region for a time domain antenna was proposed. It stated that in the far field of a time domain antenna, the peak value of the radiated transient field varies as  $R^{-1}$ , with  $R$  the distance to the virtual source of the antenna.

To get an idea of the far field region of the antennas, we have put the two antennas on boresight of each other and measured for decreasing values of  $R$  the peak value of the signal at the receiving antenna. The inverse of the value is plotted in Fig. 6-9 as a function of  $R$  and a line is fitted through the measured points. For values of  $R$  down to 30 cm the points are still on a line. This indicates that the far field region of the antennas begin at least at a distance of 30 cm from the antenna's virtual source, but probably even sooner. Unfortunately we did not perform measurements below 30 cm to determine the exact far field region. As the TEM horns guide essentially a TEM mode, it was expected that the far fields region would begin close to the antenna.

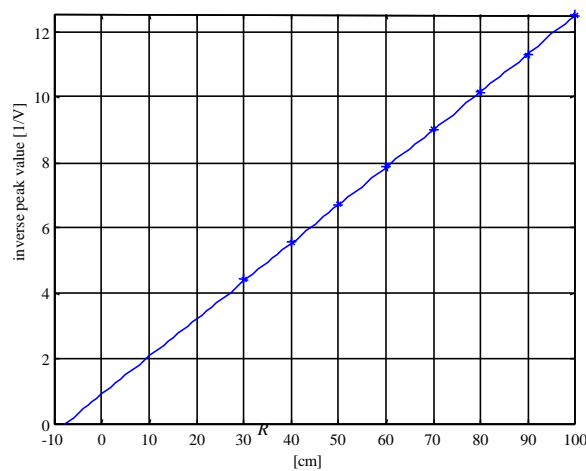


**Fig. 6-9:** Determination of the far field region of the antennas

A last parameter influencing the height of the antenna is the  $R^{-1}$  free space loss or spreading loss. Without going into detail one can intuitively understand that the closer the antennas are to the ground, the closer the antennas will be to the objects, and thus the easier it will be to detect them.

The conditions on the mobility and the far field of the antennas are in contradiction with the condition on the free space loss, so a compromise urges itself. We want the objects in the far field of the antennas, but not too far from the antennas and we want the antennas at least 20 cm above the ground to guaranty their mobility. Therefore we have chosen the height of the antennas for the laboratory UWB GPR to be 25 cm above the ground. Hence, if the targets are shallow buried, we have to keep in mind

that they will be at the under-limit of the far field of the antennas, and that the time domain model will be less accurate.

### 6.3.2. Antenna Coupling

Part of the energy radiated by the Tx antenna will directly couple into the receiving antenna, without being reflected on any object. This phenomenon is called antenna cross-coupling or in short antenna coupling. Antenna coupling can create a ringing between the two antennas. This means that the duration of the antenna coupling can be larger than the duration of the excitation pulse applied on the transmitting antenna. Therefore antenna coupling is usually also expressed as a function of time.

In principle antenna coupling is not critical and can be compensated for. Once the antenna coupling is measured (with the two antennas radiating in free space), the coupling can be subtracted from each measured A-scan. Nevertheless it is better to keep the antenna coupling as small as possible in amplitude and in duration. If the ringing between the two antennas lasts too long, it can interfere with the useful backscattered signal. Furthermore, every backscattered incoming signal on the antennas will make the antennas radiate again due to mismatches in the antenna. Hence the backscattered incoming signals will themselves be sources of ringing between the antennas, which can of course not be compensated for, since they are stochastic.

For the laboratory UWB GPR we choose to measure only the co-polarised backscattered field, *i.e.* the backscattered field in the same polarisation as the radiated field. In this case, the TEM horn antennas can be put in two trivial configurations: either they are put with a common E-plane, *i.e.* the E-field of the transmitting antenna and the receiving antenna are aligned, or they are put with a common H-plane, *i.e.* the H-field of the two antennas are aligned. The top view of the two configurations are shown schematically in Fig. 6-10.

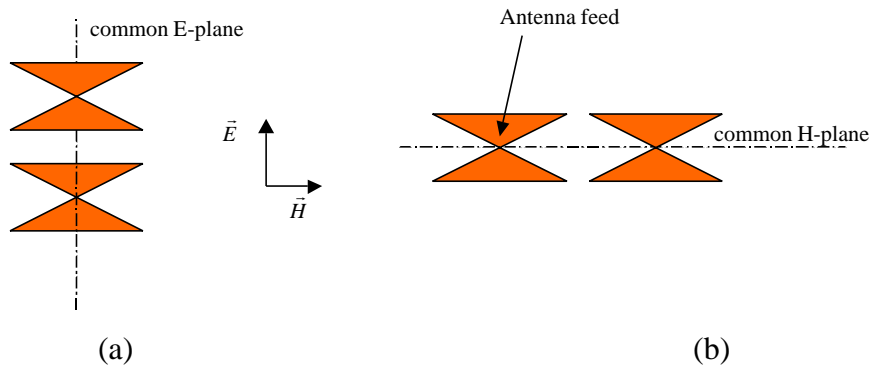


**Fig. 6-10:** (a) Top view of common E-plane configuration

(b) Top view of common H-plane configuration

In general an E-field coupling between two antennas is larger than an H-field coupling, so one could expect a larger coupling in the common E-plane configuration. This is verified with measurements. Fig. 6-11 shows in dashed line the coupling between the two antennas in the common E-plane configuration and in solid line the coupling between the two antennas with a common H-plane. In both cases the distance between the virtual sources of the two antennas was taken to be 22.8 cm. The coupling is measured as the response at the receiving antenna when the transmitting antenna is excited by a pulse. The two antennas were radiating towards RAM to avoid reflections from the surrounding structures. It is clear that the coupling in the common H-plane case is inferior in amplitude compared to the coupling in the common E-plane case. To be complete, each of these configurations can be further subdivided in two more configurations by turning one of the antennas by a  $180^\circ$ , *i.e.* the two SMA connectors pointing in the same direction or in opposite direction. As the antennas are balanced, this makes no significant difference in the amplitude nor in the duration of the coupling.

A third possible configuration is putting the Rx antennas out of the E- and H-plane of the Tx antenna. A quick test learned that this does not decrease considerably the coupling, compared to the common H-plane configuration.

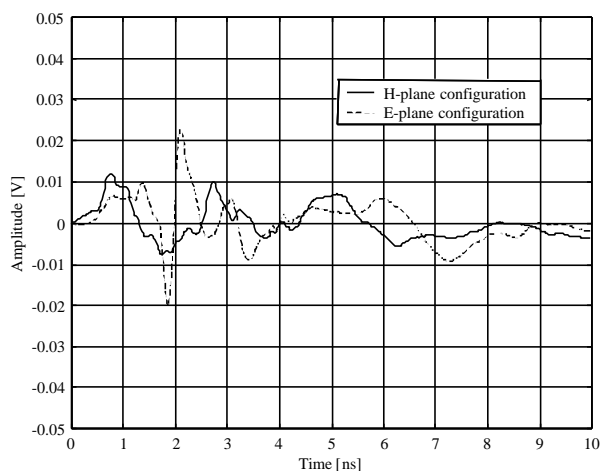


**Fig. 6-11:** Coupling between the two TEM horns in the common E-plane and common H-plane configuration

In the laboratory UWB GPR, the configuration with the lowest coupling, *i.e.* the common H-plane configuration (in solid line on Fig. 6-11), is taken. In this case the coupling will not exceed  $-27$  dB. A spectrum analysis of the coupling reveals that the H-plane coupling between the two antennas is primarily a low frequency coupling with a maximum energy around a frequency of 500 MHz. This frequency is out of the frequency range of the antennas, but has a very low reflection coefficient at the antenna feed point (see Chapter 3, Fig. 3-30), which means that the antenna will radiate around this frequency with a very low directivity.

### 6.3.3. The 3 dB footprint of the antennas

The 3 dB footprint of an antenna on a plane perpendicular to the boresight direction is defined as the region where the field, measured in the plane, is within the 3 dB of the maximum field measured in the same plane (normally on boresight of the antenna). The footprint of an antenna is schematically represented in Fig. 6-12. The footprint will be function of the height of the antenna above the plane. Fig. 6-13 shows the measured footprint of the TEM horn on a horizontal plane at 25 cm below the antenna. The footprint is 24 cm by 16 cm. The footprint was measured with a Bdot-sensor, *i.e.* a sensor that measures the time derivative of the magnetic field.

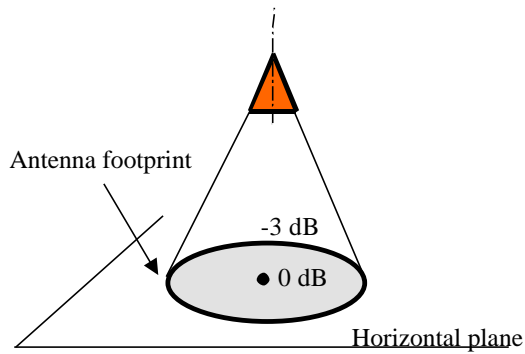


**Fig. 6-12:** Schematic representation of the antenna footprint

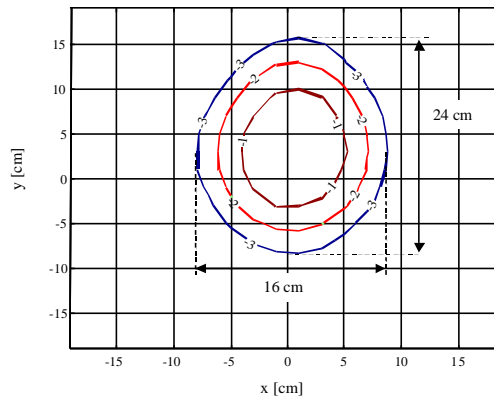


**Fig. 6-13:** Measured footprint of TEM horn

### 6.3.4. Optimisation of the antenna off-set angle

Due to the beam-width of transmit and receive antenna, a point target in the ground is already seen by the GPR system even when the point target is not exactly under the antennas. As a consequence, the reflections on the target will be smeared out over a broad region in the recorded data. However, the two-path length between the antennas and the target is larger when the target is not exactly under the antennas, hence the reflection will appear later in time, as schematically represented in Fig. 6-14. It can easily be verified that the obtained structure in the B-scan is a hyperbola (see Chapter 2). There exist a number of signal processing algorithms, called migration, which correct for this defocusing. In the ideal case, the migration algorithm will focus all the energy back into the true position and physical shape of the target.

An important parameter in the Tx-Rx antenna configuration is the combined antenna footprint – *i.e.* the footprint of the two antennas considered as one antenna. The resulting 3dB footprint of the two antennas is obviously a function of the offset angle  $\alpha_1$  as represented in Fig. 6-15. Note that a larger 3 dB footprint produces larger hyperbolas in the B-scan. The question is if this increases the detectability of objects or not.

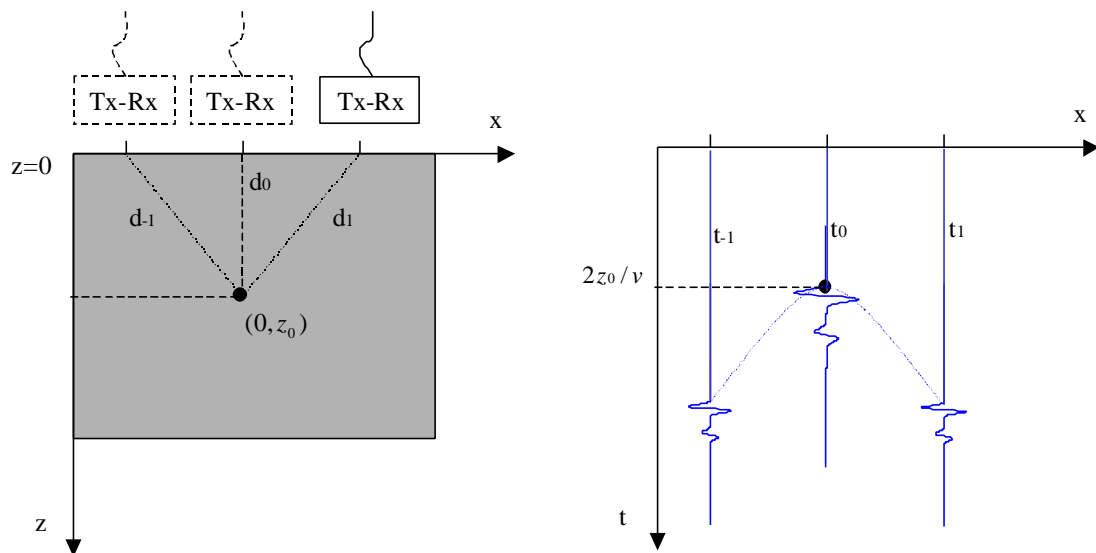


**Fig. 6-14:** Schematic representation of defocusing on a point target

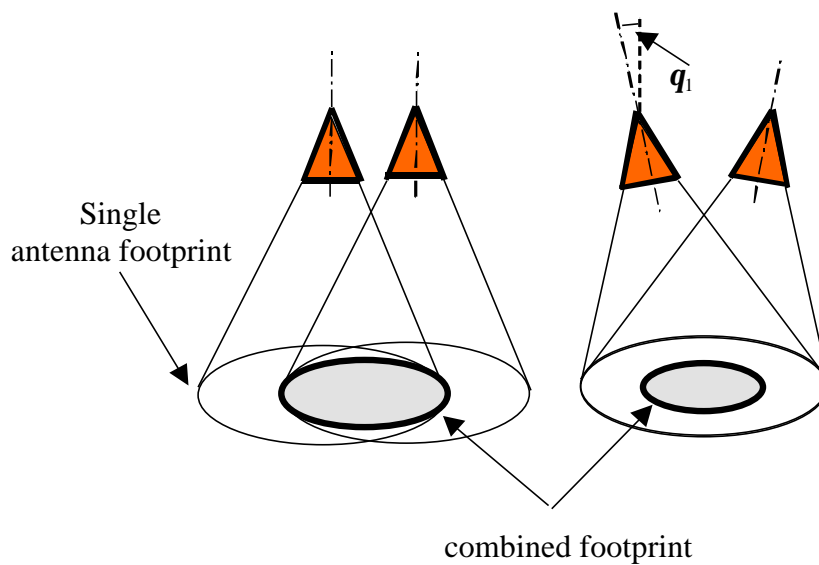


**Fig. 6-15:** Combined antenna footprint

The aim of the study in this section is to find the optimum offset angle  $q_1$  of the antennas for a given configuration, *i.e.* height of the antenna, depth of the object and soil type. As a criterion for the optimisation we consider the total energy found in the hyperbolic shaped response of a point target. This total energy represents in some sense the expected energy of the point target in a B-scan, after enhancing the B-scan by an optimal migration method. For this reason, we simulated 31 different synthetic

B-scans of a point scatterer at 6 cm in the ground, for different offset angles  $\mathbf{q}_1$  between  $0^\circ$  and  $30^\circ$  in steps of  $1^\circ$ . The fictive point scatterer is represented by a bistatic impulse response  $\Lambda = \mathbf{d}(t)$ . The configuration is shown in Fig. 6-16. For each position  $x$  between  $-50$  cm and  $50$  cm of the antenna pair, the backscattered signal  $V_{rec}(t)$  is calculated using the time domain GPR range equation (5.13). The backscattered signals  $V_{rec}(t)$  for all the antenna positions are then represented as a B-scan, as shown in Fig. 6-17. In the simulations, the transmission losses and the influence of the ground are also taken into account, although they have no influence on the interpretation of the result, as they are the same for all offset angles. Fig. 6-17 shows the result of the simulation for an offset angle  $\mathbf{q}_1 = 20^\circ$ .

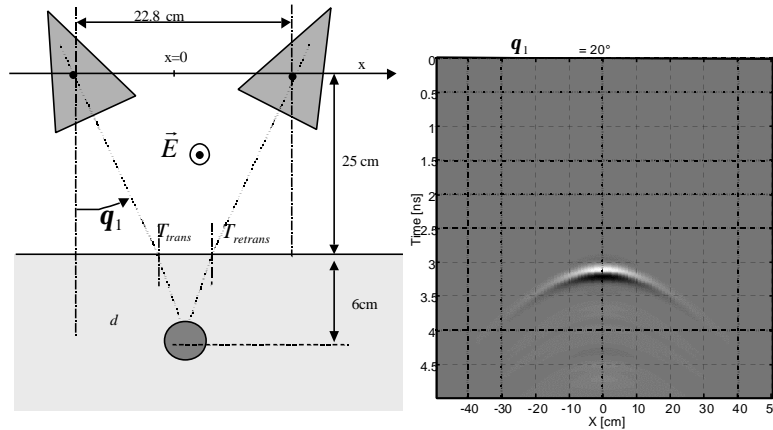


**Fig. 6-16:** Antenna configuration

**Fig. 6-17:** Synthetic B-scan for  $\mathbf{q}_1 = 20^\circ$

For each of the 31 synthetic B-scans, the total energy in the hyperbolic shaped response of the target is calculated as

$$E_{tot} = \int \int_x |V_{rec}(t)|^2 dt dx \quad (6.1)$$

Fig. 6-18 shows the total energy in the hyperbolic response of the point target as a function of the offset angle  $\mathbf{q}_1$ . The total energy in the hyperbola increases for increasing values of the offset angle. But when the offset angle becomes too large, the energy in the hyperbola decreases. The maximal energy in the hyperbola is found for

an offset angle of  $20^\circ$ , which for this configuration (object depth and soil type) corresponds to the angle that focuses the antennas on the target, taking into account the refraction. The same result is obtained for other object depths and soil types. In general we can conclude that the optimum offset angle, with respect to the total backscattered energy on a point target, is the angle that focuses the antennas on the target. Although the obtained conclusion seems trivial, it is not straightforward to confirm. The above simulation however gives an objective verification.

In reality the depth of the object is *a priori* unknown, but is expected to be between 0 and 20 cm. However, the graph in Fig. 6-18 indicates that the maximum in the energy is rather flat, meaning that the choice of the optimal offset angle is not too critical. In the design phase of the laboratory UWB GPR, a most probable depth for an AP mine of 6 cm was assumed, leading to an offset angle  $q_1$  of  $20^\circ$ .

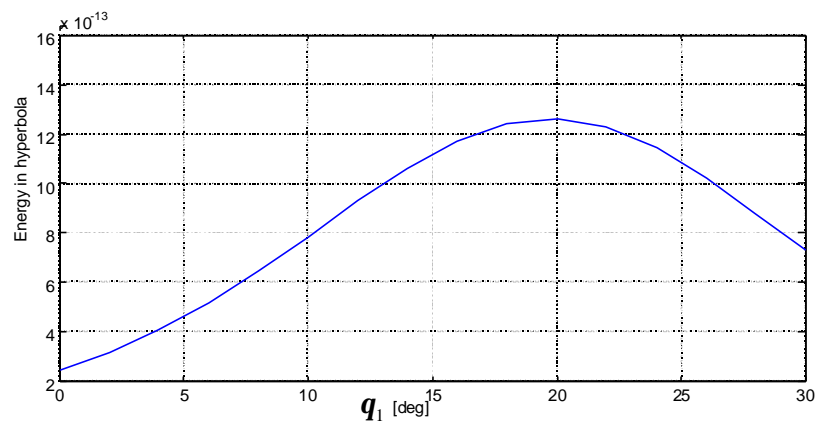


**Fig. 6-18:** Total energy in the hyperbolic shaped response of a point target at 6 cm of depth

Table 6.2 resumes the choices on the antenna configuration, resulting from the study made in this section. Fig. 6-19 shows a photo of the antenna configuration as used in the laboratory UWB GPR system.

<b>Configuration characteristic</b>	<b>Expression</b>
Preferred height of the antennas above the ground	25 cm
Distance between the two virtual sources	22.8 cm
Polarisation	H-field of the two antennas aligned (common H-plane)
Offset angle	20°

**Table 6.2:** Antenna configuration



**Fig. 6-19:** Photo of antenna configuration

## 6.4. Study of the range performance

In the design phase of a GPR system it is indispensable to study the range performance or penetration depth of the system. In the literature one can find multiple examples of such studies [2][3]. Unfortunately they all start from the radar range equation in the frequency domain. As already mentioned in the introduction of Chapter 5, describing the range performances of time domain system, using frequency dependent signal power has some drawbacks. The radar range equation contains frequency dependent terms, hence they have to be expressed over the whole frequency band of interest. Further, to estimate the range performance, one has to specify the minimum detectable signal power of the receiver at a given frequency. For a time domain system it is more practical to express the minimum detectable signal of

the receiver in terms of peak voltages instead of frequency dependent signal power. The study of the range performance of a time domain GPR system can be done with far more accuracy by modelling the whole UWB GPR in the time domain. Once the minimal detectable peak amplitude of the receiver is known, the time domain GPR range equation (5.13) can be used to calculate the range performance of the impulse radar system for a given configuration, *i.e.* soil type and target.

In this section an evaluation of the range performance is done for our laboratory UWB GPR. The range performance is studied for the following configuration: the target is a metallic sphere with a radius of 5 cm, buried in a sandy soil. The soil, coming from Cambodia, has a texture composition of 69% of sand, 24% of silt and 7% of clay. This sandy soil represents a regular agriculture soil with which deminers are confronted. The complex permittivity of the soil was measured by the UCL [4] in function of the moisture content and frequency. Table 6.3 shows the real relative permittivity, the loss tangent and the attenuation constant  $\alpha$  for 3 different moisture contents at a frequency of 2 GHz. The first two values are sufficient to calculate for each moisture content the impulse response of the soil using the analytic expression (5.26).

<b>Moisture content</b>	<b>Real relative permittivity</b>	<b>Loss tangent</b>	<b>Attenuation [dB/m]</b>
0%	2.55	0.01	2.9
5%	4.45	0.056	21.4
10%	8.16	0.085	44.1

Table 6.3: Characteristics of a sandy soil coming from a rice field in Cambodia at 2 GHz

In the study we introduced some simplifications without loss of generality. Because we are only interested in the peak value of the backscattered signal, we can replace the IR of the metallic sphere by  $\Lambda(t) = 0.314 \mathbf{d}(t)$ , representing the IR of a fictive metallic object, which is comparable to the IR of the metallic sphere with a radius of 5 cm by only taking into account the specular reflection (see also equation (5.35)). Further we assume that the bistatic RCS of the target is independent of the bistatic

angle and that the air-ground interface is flat. A schematic representation of the configuration for the study of the range performance is shown in Fig. 6-20. The virtual source of the antennas are at 25 cm from the ground and the two antennas are separated by 22.8 cm. The air-ground interface is at  $z = 0$ . The excitation waveform  $V_s(t)$  is the Gaussian pulse generated by the step generator, followed by the impulse-forming network (Fig. 6-4).

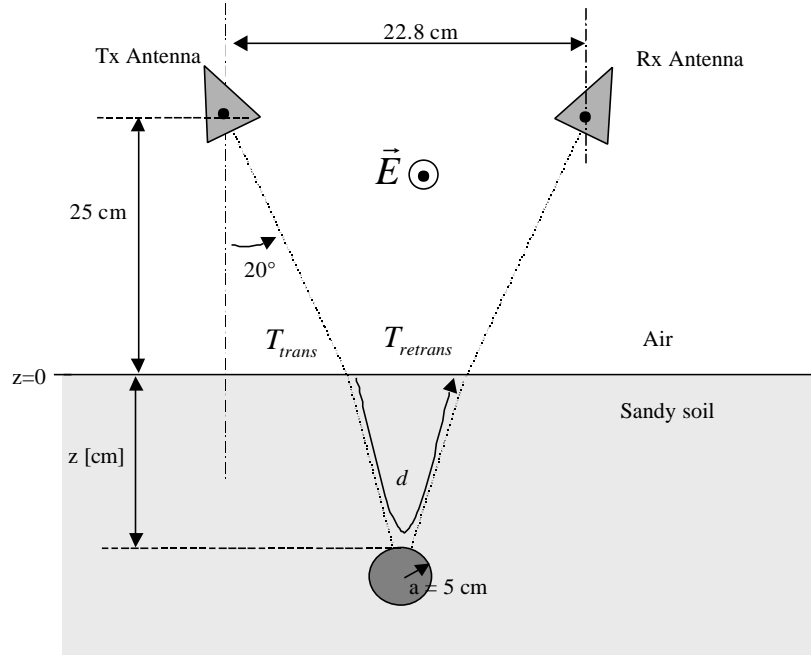


**Fig. 6-20:** Configuration for range performance

First, for a given target depth and moisture content, the backscattered signal  $V_{rec}(t)$  is calculated using equation (5.13). Fig. 6-21 shows as an example the simulated backscattered signal for the target at a depth of 5 cm and moisture content of 0%. From this signal, the peak amplitude is taken and expressed in dBm as

$$V_{rec,peak} [dBm] = 10 \log \left( \frac{V_{rec,peak}^2 [Volt] 10^3}{50} \right) \quad (6.2)$$

$V_{rec,peak}^2 [Volt]/50$  corresponds with the maximum instantaneous peak power of the signal. In our example the peak amplitude of the backscattered signal is 8.6 mV or –28 dBm.

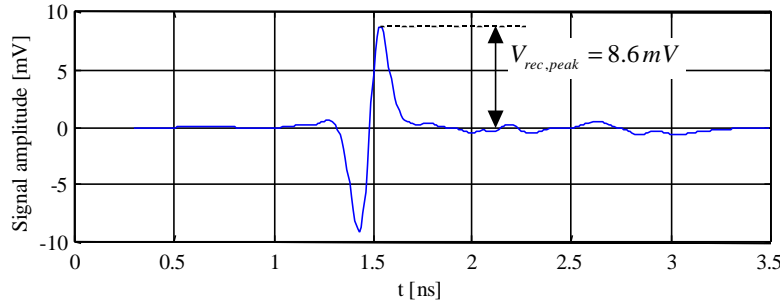


**Fig. 6-21:**  $V_{rec}(t)$  for the target at a depth of 5 cm and a moisture content of 0%.

This is repeated for all target depths and moisture contents. The results are globalised in Fig. 6-22, showing the maximum signal amplitude in dBm, at the receiver of the UWB system as a function of depth of the metallic sphere in a lossy sandy soil.

The minimal peak amplitude that can be detected by the receiver is in general limited by its noise performance. For the 6 GHz oscilloscope the RMS value of the random channel noise is measured to be less than 1mV or –47 dBm. This measurement is done according to the test procedures of the supplier, by measuring two times the same input signal, one without averaging and one with averaging 128 times, subtracting these two measurements and calculating the RMS value of the subtraction. Assuming that the noise is a white noise, the noise level of the receiver can be improved by averaging. Averaging  $N$  times improves the noise level by

$$20\log(\sqrt{N}) \quad (6.3)$$

For example, averaging 32 times, which is commonly used for GPRs, improves the noise level with 15 dB. According to Skolnik [5], for a probability of detection of 99% and a false alarm rate of  $10^{-5}$ , a signal-to-noise ratio of 14 dB is needed. If we

apply the same ratio to our time domain receiver, the minimal detectable peak amplitude of the 6 GHz oscilloscope, with 32 times averaging, will be

$$-47 \text{ dBm} - 15 \text{ dB} + 14 \text{ dB} = \mathbf{-48 \text{ dBm}}$$

The determination of the minimal detectable peak amplitude of a receiver is quite subjective and can be source of discussion. In practice the minimal detectable peak amplitude depends on more factors than the noise floor of the receiver only. For instance the ringing in the antennas or the residual cross-coupling between the antennas after compensation, exceeding the level of  $-48 \text{ dBm}$ , could possibly mask small reflections on targets. On the other hand the above reasoning is done for the GPR system in one physical position. Normally, the GPR is used to acquire B- or C-scans. In this case a point target will generate a hyperbolic response in the image, which could increase the detectability of the object. Further, signal processing techniques on the B- or C-scans will also increase the detectability of targets. It is difficult to estimate the total influence of all these factors on the minimal detectable peak amplitude, therefore in this example we only take into account the noise performance of the receiver.

Once the minimal detectable peak amplitude of the receiver is determined, the maximum range at which the target can be detected can be read from the plot in Fig. 6-22. Doing so, one of the main disadvantages of an UWB GPR clearly appears. For the same sandy soil, the maximal range (penetration depth) decreases from 50 cm when the soil is dry over 20 cm when the soil has a moisture content of 5% to only 11.5 cm for 10 % moisture content. Note that the range performances of our laboratory UWB GPR system could be increased by replacing the driving source  $V_s(t)$ . For the moment the driving source is limited to a maximum amplitude of only 2.5 V and does not make use of the full dynamic range of the receiver. Further the performance can be increased by increasing the bit resolution of the receiver and by integrating a time varying gain.

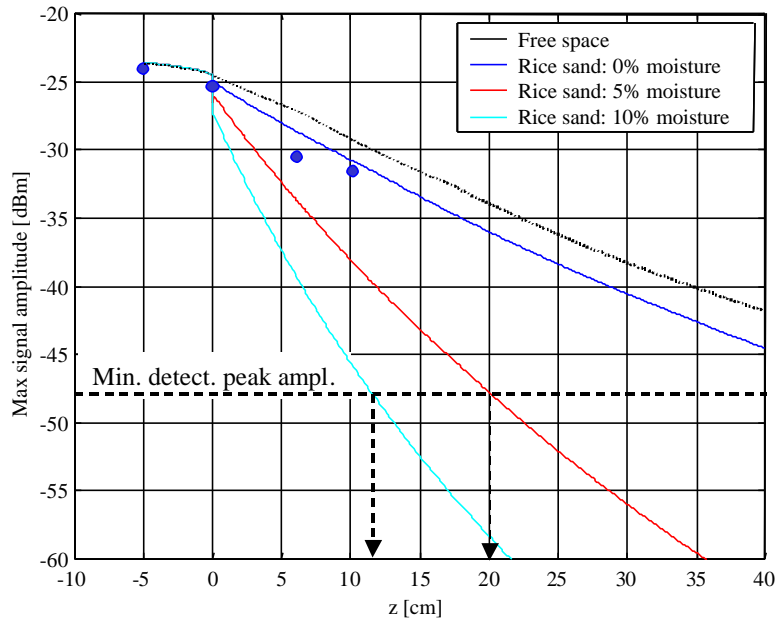


**Fig. 6-22:** Peak amplitude of the reflection on the target [dBm] as a function of the depth  $z$  [cm] for a sandy soil with respectively 0%, 5% and 10% moisture content

In the beginning of this section we stated that the range performance of a time domain GPR could be done with more accuracy by using the time domain GPR range equation. To give an idea of the accuracy of the time domain model we performed measurements on a metallic sphere with a radius of 10 cm according to the measurement set-up as shown in Fig. 6-20. The metallic sphere was buried at respectively  $z = -5$  (top of the sphere at 5 cm above the ground level),  $z = 0$ ,  $z = 6.2$  and  $z = 10.2$  cm in dry sand (0% moisture content). The dry sand is characterised by a permittivity and loss tangent that is comparable with the sandy soil used for the calculations. For each depth the peak amplitude was measured and plotted on Fig. 6-22. The calculated curve for the 0% moisture case (in blue) overestimates a little the measurement points, but the largest difference, found for the dept of 6.2 cm, does not exceed 2 dBm.

## 6.5. Experimental results

### 6.5.1. Acquisition software

For the acquisition of the data, two software programs have been developed: one for a B-scan and one for a C-scan. The programs control, via a serial connection, the position of the xy-table, collect the data (A-scan) from the oscilloscope via a GPIB connection and provide the man-machine-interface toward the user. Further the software allows the user to visualise the data, to perform basic signal and image processing and to save the data to disk. The data is taken on a regular grid, where the step in x- and y-direction is set by the user. Before the acquisition starts, the programs asked for a compensation of the antenna coupling. The user must put a RAM under the antennas to simulate the free space. In this case only the antenna coupling is measured. The program takes one acquisition and will keep this acquisition to subtract it from all future taken A-scans to compensate for the antenna coupling. Fig. 6-23 shows the user interface of the program for the acquisition of B-scans.

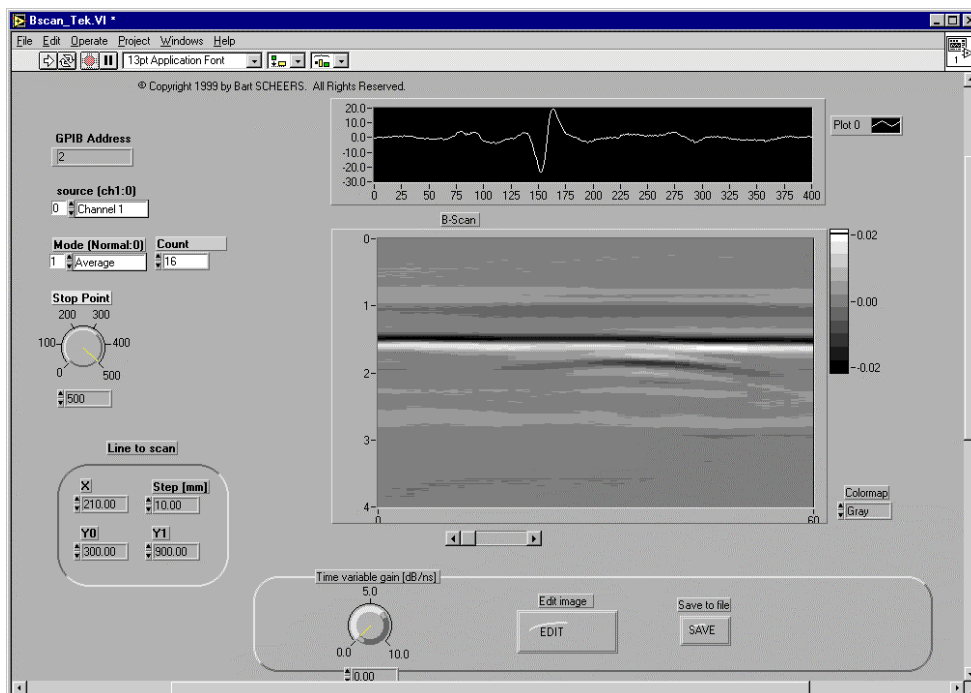


**Fig. 6-23 :** User interface of the program for the acquisition of B-scans

### 6.5.2. Results

The system can now be used to acquire B-scans and C-scans of AP mines. At this point we can already draw some conclusions concerning the advantages and disadvantages of the UWB approach. In the next three figures we show B-scans taken by the laboratory UWB GPR. On the horizontal axis the displacement of the antennas is given in centimetres; the vertical axis represents the time in ns. The images represent raw data, so no signal processing was performed on the data, except for the compensation of the antenna coupling.

Fig. 6-24 shows an Italian VS/50 AP mine buried in sand at a depth of 2 cm. The mine appears very clearly on the image and can be distinguished from the air-ground interface despite of the fact that it is shallow buried. With a conventional GPR system, the echo of the air-ground interface would mask the echo coming from the mine and additional signal processing would be needed to recover the target in the image. We can conclude that the UWB GPR is capable of detecting shallow buried objects.

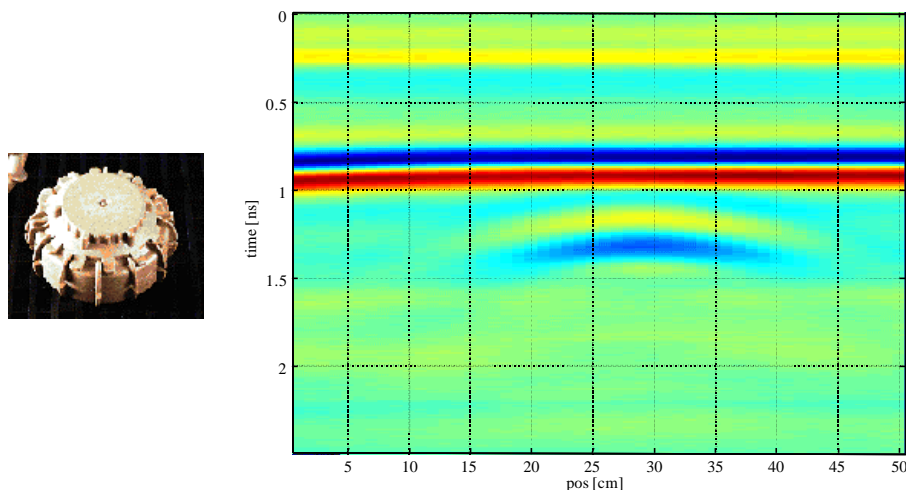


**Fig. 6-24 :** VS/50 mine buried in sand at a depth of 2 cm

In the next two figures, we show a PMN mine buried in loam a depth of 5 cm. In the first case, shown in Fig. 6-25, the loam is moistened. As expected, the signal is strongly attenuated in the wet soil and the mine is hardly visible. We then waited for two days to give the ground time to dry and took a B-scan of the same scenario again.

The result is shown in Fig. 6-26. The PMN mine is now more visible. This qualitative test demonstrates that the performances of the UWB GPR decrease dramatically in wet soils. One can compensate for the attenuation by the ground by a time-varying gain in the receiver part of the system. This is usually done in commercial GPR systems. In an oscilloscope however, this option is not available. The result can also be improved by bringing the antennas closer to the ground. Lowering the antennas means reducing the antenna footprint on the ground, so more energy will be reflected by the small mine. Reducing the antenna footprint can also be done by making antennas with a larger antenna aperture. But this means larger and heavier antennas, which is in contradiction with our design goals.

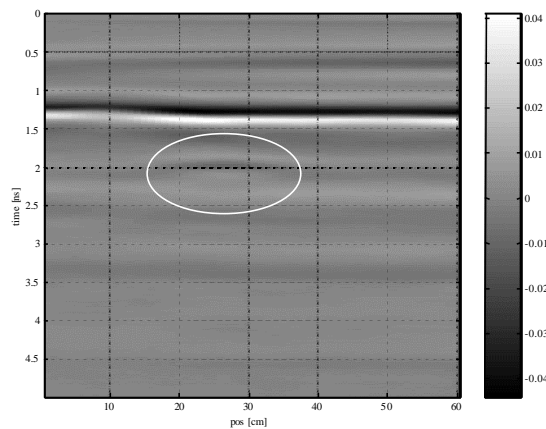


**Fig. 6-25:** PMN mine buried in wet loam a depth of 5 cm

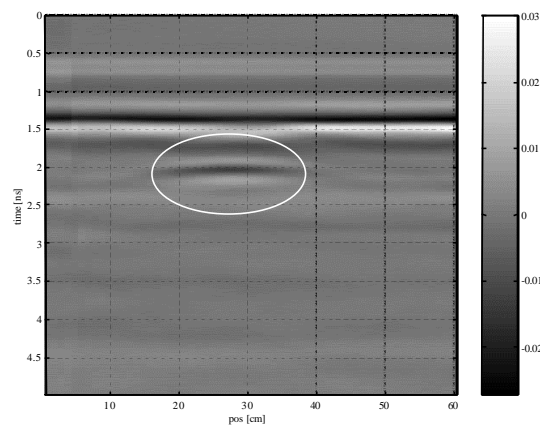


**Fig. 6-26:** Same PMN mine as in previous figure after two days

In none of the above B-scans the signature of a mine is visible. From these images of the raw data it is already clear that for classification of the object some signal and/or image processing will be needed.

## 6.6. Summary

In the frame of this research we have built a relatively simple UWB GPR systems, using mainly off-the-shelf equipment. The system can be mounted on a xy-table for indoor trials or on a robot for outdoor trials. The main purpose of this system was to provide the group with UWB data on AP mines. Further it gave the opportunity to evaluate the time domain model. Measurements on a metallic sphere showed a good correspondence with the simulations. Some shortcomings of the UWB GPR system are the weak instantaneous power in the impulse (maximum amplitude of 2.5 V) and the lack of a time varying gain in the receiver part.

The antenna configuration of the UWB GPR was studied in detail using the time domain radar range equation. The study revealed that the optimal offset angle for the antennas is the one that focuses the antennas on the target. In this case, the total reflected energy on a point target could become several times larger than when the two antennas have their boresight parallel to each other. Further the range performance of the system was investigated for a given target in a given soil. The range performance of a time domain GPR was found to be very accurate by using the time domain GPR range equation. From this study we could conclude that the range performance of the UWB system will be limited by the moisture content of the soil. This is due to the dramatically increasing attenuation of the radiated signal by the soil as a function of frequency and moisture content. In a sandy soil with a moisture content of 10 %, the UWB GPR can detect a metallic sphere with a radius of 5 cm down to a burial depth of only 11.5 cm.

Some tests were done on AP mines. At this point we can already draw some preliminary conclusions concerning the advantages and disadvantages of the UWB approach. First of all, as expected the tests showed the capability of detecting

shallowly buried mines. The tests also confirmed that when mines are buried deeper and the soil has a high moisture content, the visual detection becomes almost impossible.

Although the data on the targets has a better depth resolution and contains more frequency information on the target, the visual classification of objects in the B- and C-scans is not feasible. However, this extra information is present in the data and can hopefully be explored using advanced signal and image processing algorithms like time-frequency analysis and analysis of resonance in the late time response of the objects.

## REFERENCES

- [1] M. Piette, *Banc de mesure en régime transitoire de la signature radar d'objets tridimensionnels*, Doctoral thesis, Université catholique de Louvain and Royal Military Academy, Belgium, Oct. 1995.
- [2] D. J. Daniels, *Surface Penetrating Radar*. London: IEE, 1996, pp. 11-18.
- [3] J. L. Davis and A. P. Annan, "Ground-Penetrating Radar for High-Resolution Mapping of Soil and Rock Stratigraphy", *Geophysical Prospecting*, vol. 37, pp. 531-551, 1998.
- [4] M. Storme, I. Huynen and A. Vander Vorst, "Characterization of wet soils in the 2-18 GHz frequency range," *Microwave and optical technology letters*, vol. 21, no. 5, June 1999.
- [5] M. Skolnik, *Radar handbook*. New York: McGraw-Hill, 1990, p. 2.20.

